


# Sun-as-a-star observations of the 2017 August 21 solar eclipse

Ekaterina Dineva<sup>1,2</sup>, Carsten Denker<sup>1</sup>, Meetu Verma<sup>1</sup>,  
Klaus G. Strassmeier<sup>1,2</sup>, Ilya Ilyin<sup>1</sup> and Ivan Milic<sup>3</sup>

<sup>1</sup>Leibniz-Institut für Astrophysik Potsdam (AIP), An der Sternwarte 16,  
14482 Potsdam, Germany  
email: [edineva@aip.de](mailto:edineva@aip.de)

<sup>2</sup>Universität Potsdam, Institut für Physik und Astronomie, Karl-Liebknecht-Str. 24/25,  
14476 Potsdam, Germany

<sup>3</sup>University of Colorado Boulder, Laboratory for Atmospheric and Space Physics,  
1234 Innovation Drive, Boulder, CO 80303-7814, U.S.A.

**Abstract.** The Potsdam Echelle Polarimetric and Spectroscopic Instrument (PEPSI) is a state-of-the-art, thermally stabilized, fiber-fed, high-resolution spectrograph for the Large Binocular Telescope (LBT) at Mt. Graham, Arizona. During daytime the instrument is fed with sunlight from the 10-millimeter aperture, fully automated, binocular Solar Disk-Integrated (SDI) telescope. The observed Sun-as-a-star spectra contain a multitude of photospheric and chromospheric spectral lines in the wavelength ranges 4200–4800 Å and 5300–6300 Å. One of the advantages of PEPSI is that solar spectra are recorded in the exactly same manner as nighttime targets. Thus, solar and stellar spectra can be directly compared. PEPSI/SDI recorded 116 Sun-as-a-star spectra during the 2017 August 21 solar eclipse. The observed maximum obscuration was 61.6%. The spectra were taken with a spectral resolution of  $\mathcal{R} \approx 250\,000$  and an exposure time of 0.3 s. The high-spectral resolution facilitates detecting subtle changes in the spectra while the Moon passes the solar disk. Sun-as-a-star spectra are affected by changing contributions due to limb darkening and solar differential rotation, and to a lesser extent by supergranular velocity pattern and the presence of active regions on the solar surface. The goal of this study is to investigate the temporal evolution of the chromospheric Na D doublet during the eclipse and to compare observations with synthetic line profiles computed with the state-of-the-art Bifrost code.

**Keywords.** Sun: chromosphere, instrumentation: spectrographs, techniques: spectroscopic, methods: data analysis

---

## 1. Introduction

Data collected during solar eclipse observations provide valuable input for studies of the outer atmosphere of the Sun including the chromosphere (Athay 1976). Its name originates from the red flash of H $\alpha$  emission, which appears within the totality phase. The chromosphere is an intermediate layer between the relatively cool photosphere and the million-degree corona. The physical boundaries of this intermediate layer are in the range 500–5000 km above the solar surface (Vernazza *et al.* 1981; Rutten 2007) but the chromosphere is highly structured, both horizontally and vertically, e.g., spicules, motes, rosettes, and various kinds of filaments, so that an exact definition of its borders is difficult and maybe not even appropriate. Aimanova & Gulyaev (1976) derived the formation height among other height-dependent properties of the Na I D doublet, using slitless spectrograms of the 1976 July 10 total solar eclipse over Chukotka, Russia.

The obscuration of the solar disk by the Moon presents a unique setting for researchers to address a broad range of topics (Pasachoff 2009). Major parts of eclipse research concern the corona (e.g., Saito & Tandberg-Hanssen 1973; Habbal *et al.* 2011; Koutchmy *et al.* 2019). However, observations in the visible spectrum, as well as in the adjacent infrared (IR), ultraviolet (UV), and extreme ultraviolet (EUV) bands, are popular in solar physics (e.g., Dunn *et al.* 1968; Bazin & Koutchmy 2013), solar-stellar connection studies (Schleicher *et al.* 2004), and exoplanet research (e.g., Takeda *et al.* 2015; Reiners *et al.* 2016). Albeit rarely in the focus of eclipse observations, manifestations of magnetic activity are interesting because they affect the radial velocity measurements of active stars (Haywood *et al.* 2016; Cauley *et al.* 2018, e.g.,). Although the Sun is not an extremely active star, only the solar case delivers detailed knowledge about the evolution and properties of the active regions (e.g., Verma *et al.* 2016; Verma 2018). Supported by models of stellar atmospheres (Beeck *et al.* 2012), the above studies have two significant outcomes, i.e., an improved understanding of the underlying physical processes and additional input information to increase the precision of models.

The chromosphere is highly dynamics and feature-rich. Observing the Sun in various strong chromospheric absorption lines, e.g.,  $H\alpha$ ,  $Ca\ II\ K\ \&\ H$ , and the infrared  $Ca\ II$  triplet, allows us to investigate the fine structure as well as the global behaviour of the solar chromosphere. The solar alkali spectrum, in particular Sodium  $Na\ I\ D\ \lambda 5890\ \text{\AA}$  and Potassium  $K\ I\ \lambda 7699\ \text{\AA}$ , gain significant popularity in solar and stellar research (e.g., Nikolov *et al.* 2016; Lendl *et al.* 2017). For example, conveniently used in helioseismology (Bruls *et al.* 1992), the  $Na\ I\ D$  doublet offers diagnostics tools linking photospheric and lower chromosphere dynamics (Leenaarts *et al.* 2010).

During the 2012 May 21 solar eclipse, Takeda *et al.* (2015) obtained 184 disk-integrated spectra of with the High Dispersion Echelle Spectrograph (HIDES, Izumiura 1999) at the Okayama Astrophysical Observatory, Japan. The high-resolution spectra ( $\mathcal{R} \approx 520\ 000$ ) covered the wavelength range 4400–7500  $\text{\AA}$ . An exposure time of 10 s made it possible to trace the eclipse with very good temporal resolution. Deriving the latitude dependence of the solar differential rotation was the primary goal of this study. Thereby, the Sun served as a template that can be utilized in the analysis of stellar radial velocity curves, deriving sensitive information about stellar systems, star-planet interactions, and eclipsing binaries and their rotational parameters.

In the spirit of the aforementioned study, Reiners *et al.* (2016) investigated the the properties of disk-integrated photospheric absorption line spectra observed during the 2015 March 20 solar eclipse. Employing a Fourier Transform Spectrometer (FTS, Davis *et al.* 2001) at the 50-cm Vacuum Vertical Telescope (VVT) of the Institut für Astrophysik, Göttingen (IAG), they obtained 159 disk-integrated spectra of the eclipse in two spectral ranges, i.e., 5000–6200  $\text{\AA}$  and 6500–6700  $\text{\AA}$ . Similar to the observations by Takeda *et al.* (2015), the Göttingen eclipse was not on the path of totality, which is however irrelevant in the context of exoplanet research. Reiners *et al.* (2016) analyzed the velocity curves computed from the eclipse spectra and quantified all solar contributions. Thus, the crucial impact of the convective blueshift was revealed and the need for more realistic models was demonstrated.

The studies by Takeda *et al.* (2015) and Reiners *et al.* (2016) motivated our investigation of the  $Na\ I\ D$  doublet during the 2017 August 21 solar eclipse and the modeling of these strong chromospheric absorption lines based on magneto-hydrodynamics (MHD) simulations. Additional impetus arises from the strong interest in the behavior of the Fraunhofer lines within the stellar and exoplanet research communities (Czesla *et al.* 2015), in particular provoked by the  $Na\ I\ D$  abundance in the atmospheres of hot Jupiter planets (Yan *et al.* 2015).

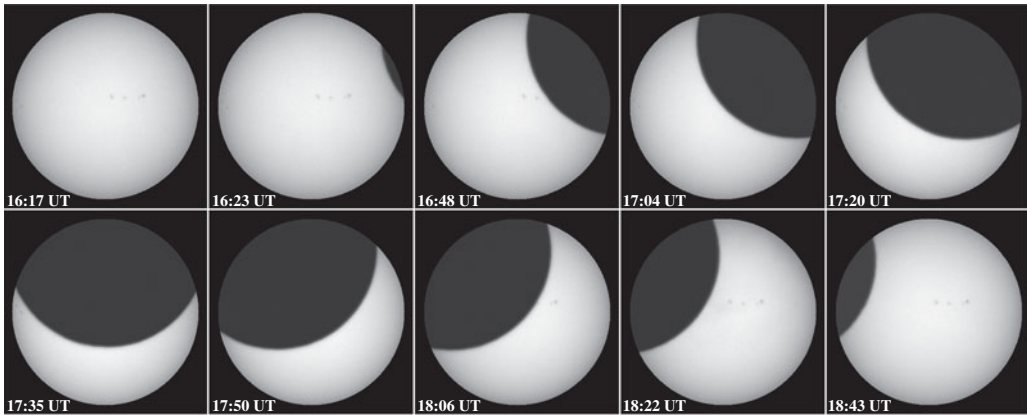


**Figure 1.** Full-disk broad-band images observed with the SDI guiding telescope during the 2017 August 21 solar eclipse. Active regions NOAA 12671 and 12672 are visible near disk center and at the eastern limb, respectively.

## 2. Observations and data reduction

The 2017 August 21 total solar eclipse was only visible as a partial eclipse at Mt. Graham Observatory, Arizona, U.S.A. The partial eclipse started at 16:17 UT and ended at 19:06 UT, while the maximum obscuration (61.6%) took place at 17:38 UT, i.e., the elevation of the Sun rose from  $42.6^\circ$  to  $68.8^\circ$  during the eclipse, which corresponds to an air mass of 1.48 at the beginning of the eclipse and about unity at its conclusion. More details of solar eclipses can be obtained from the Solar Eclipse Computer (SEC) provided by the U.S. Naval Observatory (Bartlett *et al.* 2019). Due to technical problems with the telescope drive between 16:23 and 16:49 UT, a chunk of data is missing. Increasing overcast towards the end of the eclipse terminated observations after 18:43 UT. Overall, however, the weather and seeing conditions were favorable during the eclipse.

The Potsdam Echelle Polarimetric and Spectroscopic Instrument (PEPSI, Strassmeier *et al.* 2015, 2018) was designed to record stellar spectra with a spectral resolution of up to  $\mathcal{R} \approx 250\,000$ , exploiting the light gathering capability of the  $2 \times 8.4$ -meter diameter Large Binocular Telescope (LBT, Hill *et al.* 2006). The 10-millimeter diameter Solar-Disk Integrated (SDI) telescope is located on the LBT's kitchen balcony. It observes the Sun as a star, feeding a pair of  $300\ \mu\text{m}$ -core fibers that guide the light to the blue and red arm of the spectrograph, while a small full-disk telescope provides accurate guiding. Selected full-disk images tracing the evolution of the eclipse are shown in Figure 1. The time-series contains more than 800 full-disk images at a cadence of 10 s. Two small active regions (NOAA 12671 and 12672) were present on the disk, one at disk center and one near the eastern limb, which were successively concealed by the passing Moon.

In a dedicated observing campaign during the solar eclipse, 116 high-resolution spectra were obtained with PEPSI/SDI, covering the two spectral spectral windows 4200–4800 Å and 5300–6300 Å with an average dispersion of 2 mÅ. An exposure time of 0.3 s followed by a CCD readout time of 40–60 s, yields a cadence of approximately 60 s between consecutively acquired observation. The average signal-to-noise (S/N) ratio is approximately 700:1 for a single exposure. Stacking spectra to improve the S/N ratio is not an option because a good temporal resolution is needed to track the evolution of the eclipse.

In the present study, we investigate the temporal evolution of the solar Na I D doublet during the eclipse. Facilitated by the eclipse geometry, the 116 high-resolution spectra provide snapshots with different contributions from solar differential rotation and limb darkening. In the top panel of Figure 2, we display a “quiet-Sun” Na I D spectrum  $I_{\text{QS}}(\lambda)$ ,

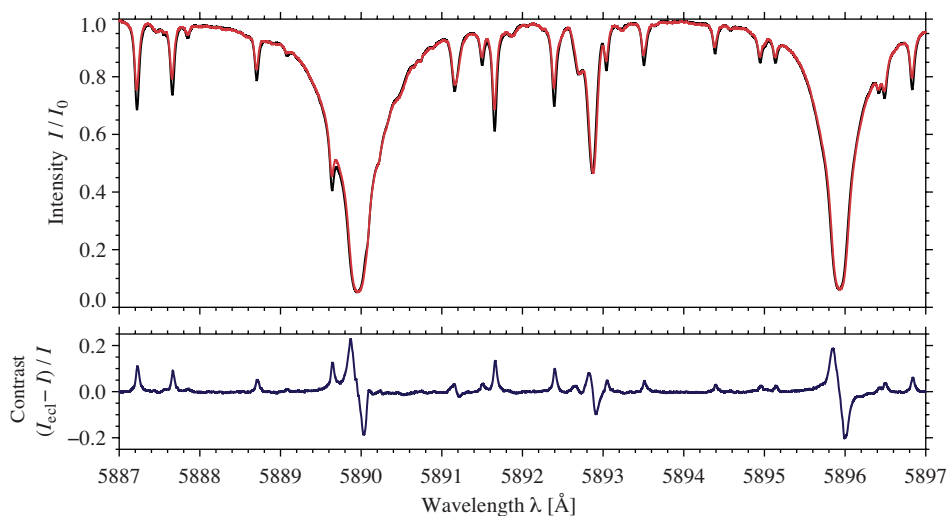


**Figure 2.** Sun-as-a-star intensity profiles of the chromospheric Na I D doublet (*top*). This spectral range was extracted from a PEPSI/SDI spectrum covering the spectral window 5300–6300 Å. A spectrum  $I(\lambda)$  before the eclipse (*blue*) is compared with a spectrum  $I_{\text{ecl}}(\lambda)$  recorded at 18:06 UT (*red*), i.e., close to the culmination of the eclipse. Both spectra were normalized so that the continuum intensity  $I_0$  corresponds to unity. The contrast profile was computed according to Equation 2.1 and exhibits signals of up to 20% of the local intensity.

which was recorded just before the onset of the eclipse. An eclipse Na I D spectrum  $I_{\text{ecl}}(\lambda)$  is shown for comparison. The differences are small and hard to detect by visual inspection. Some telluric lines exhibit a variation of line depth during the eclipse, which can be attributed to the decreasing air mass. The sample eclipse spectrum was selected 27 min after the culmination of the eclipse because the eclipse geometry will produce a spectrum at maximum obscuration that is almost indistinguishable from the quiet-Sun profile, besides the lower intensity. Computing contrast profiles (see bottom panel of Figure 2) will enhance and quantify the eclipse signal according to

$$C(\lambda, t) = \frac{I_{\text{ecl}}(\lambda, t) - I_{\text{qS}}(\lambda)}{I_{\text{qS}}(\lambda)}. \quad (2.1)$$

After the culmination of the eclipse, the shape of contrast profile resembles that of the derivative of a Gaussian, with the positive lobe at shorter wavelengths. The peak-to-valley (PTV) contrast difference is 0.41. Before the eclipse both lobes change sign. An inclination of the Moon's path with respect to solar North-South will lead to an asymmetry of minima and maxima of the contrast profiles and also affect the wings.

Despite the minimum of Solar Cycle 24, two small active regions were present, which will however not significantly affect the spectral profiles. The Moon started to cover the spots of active region NOAA 12671 at 16:45 UT, completely covered them at 16:48 UT, and uncovered them at 18:15 UT. Due the location of active region NOAA 12672 near the eastern limb, the first spot was covered at 17:41 UT. Observing its reemergence was obstructed by clouds. The presence of sunspot groups facilitated the proper alignment of the images taken by SDI, which in turn confirmed the eclipse geometry. The impact of active regions was neglected in the later comparison with the contrast profiles derived from Bifrost simulations (Section 3). In principal, the time-dependent supergranular velocity pattern will also affect the spectral profile but in the comparison, we

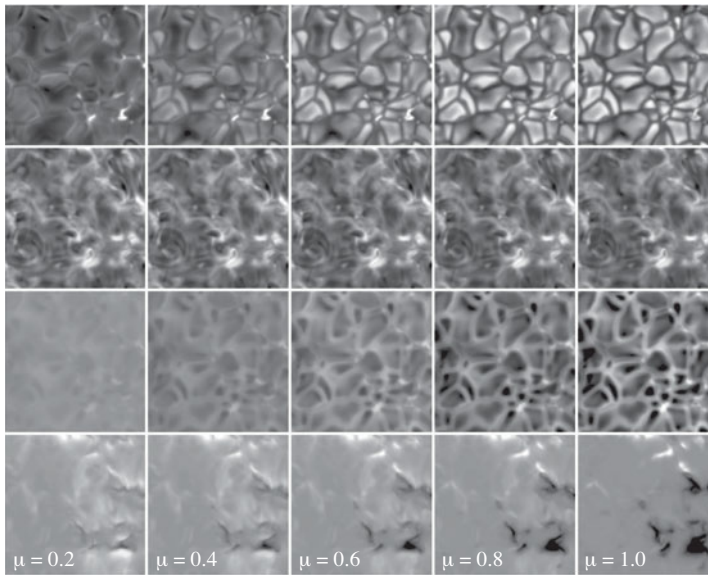


**Figure 3.** Center-to-limb variation (*left to right*) of a network element in the quiet Sun based on a Bifrost simulation. Displayed are emergent continuum intensity, line-core intensity, center-of-gravity velocity, and maximum degree of circular polarization (*top to bottom*), which were derived from the strong chromospheric absorption line  $\text{NaD}_2$ . The intensities are scaled for clarity, and the line-core intensity is shown on a logarithmic scale. The velocity is scaled between  $\pm 2 \text{ km s}^{-1}$  and the degree of polarization between  $\pm 20\%$ .

limited the velocity distribution across the disk to solar differential rotation including the accurate  $B_0$ -angle (heliographic latitude of the central point of the solar disk).

### 3. Contrast profiles derived from Bifrost simulations

Bifrost is a state-of-the-art parallel numerical code for MHD simulations of stellar atmospheres from the convection zone to the corona (Gudiksen *et al.* 2011). The version employed in this study builds on many generations of numerical codes, e.g., the Oslo Stagger code. Five spatio-spectral data cubes of the  $\text{NaID}$  doublet describe the CLV of a quiet-Sun region containing a strong magnetic network element. The cosine of the heliocentric angle corresponds to  $\mu = 0.2, 0.4, 0.6, 0.8,$  and  $1.0$ . The full Stokes vector is available for each of the  $200 \times 200$  pixels. The Stokes profiles are sampled at  $1 \text{ m\AA}$  covering a  $10 \text{ \AA}$ -wide spectral window in the range  $5887\text{--}5897\text{\AA}$ . The simulated spectra contain the  $\text{NaID}$  doublet as well as the photospheric  $\text{FeI } \lambda 5892.7 \text{ \AA}$  and  $\text{NiI } \lambda 5892.9\text{\AA}$  lines. In Figure 3, we present the CLV of four physical parameters describing the  $\text{NaID}_2$  line, i.e., emergent continuum intensity, line-core intensity, line-of-sight (LOS) velocity, and degree of circular polarization. The field-of-view (FOV) contains a strong magnetic network element in the lower right corner embedded in a quiet-Sun background. Ideally, such simulations would blanket the entire solar surface. This, however, will require immense computational efforts and does not take into account the three-dimensional nature of an atmosphere in a spherical shell encompassing the entire Sun. Thus, some simplifications are needed.

The goal is to model the PEPSSI/SDI Sun-as-a-star spectra of the eclipse with those derived from Bifrost simulations. In a first step, the  $200 \times 200$  Stokes- $I$  spectra are averaged for each of the five spatio-spectral data cubes. Our model Sun has a diameter of 1024 pixels, and for each pixel on the disk a spectrum is needed, which is appropriate

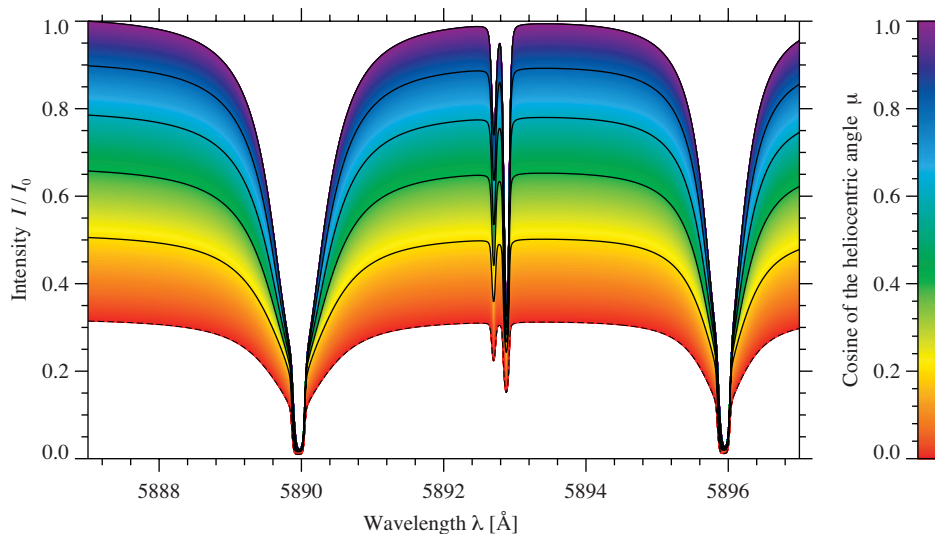


**Figure 4.** Center-to-limb variation of spatially averaged intensity profiles of the Na I D doublet, which is based on the Bifrost simulation shown in Figure 3. The initial five profiles (*solid lines*) correspond to a different value of the cosine of the heliocentric angle  $\mu = 0.2, 0.4, 0.6, 0.8,$  and  $1.0$ . The  $\mu = 0.0$  profile (*dashed line*) is a scaled version of the  $\mu = 0.2$  profile adjusted for the CLV of the continuum intensity. The six intensity profiles of the Na I D doublet are the basis for an interpolation to an equidistant grid in  $\mu$  with a resolution of  $\delta\mu = 0.001$ . The intensity profiles of the Na I D doublet are plotted with increasing distance from disk center (*violet to red*).

for a given  $\mu$  and the Doppler shift due to solar differential rotation at the given location. Active regions and the imprint of the supergranular velocity pattern are currently neglected. Thus, in a second step, the five average Na I D profiles were interpolated to an equidistant grid in  $\mu$  with a grid spacing of  $\delta\mu = 0.001$ . Since no Na I D profiles are available for  $\mu < 0.2$ , we just scaled the profile for  $\mu = 0.2$  with an appropriate CLV value of the continuum intensity. The results of this interpolation step are summarized in Figure 4.

Finally, we computed disk-integrated spectra for the eclipse with a time step of 1 min using the exact eclipse geometry at the Mt. Graham Observatory. As mentioned in Section 2, the differences are better seen in contrast profiles. A disk-integrated quiet-Sun profile without any obscuration served as the reference profile. Each disk-integrated eclipse spectrum was normalized such that the continuum intensity is unity. In principle, model light curves can be computed for continuum and line-core intensity. Signals in the contrast profiles are detected at the  $10^{-5}$  level already one minute after the start of the eclipse, which is comparable to the signal from a Mercury transit. The results of this modeling effort are plotted in Figure 5 for every second computed contrast profile. The red-blue color coded spectra vary smoothly from the start to the end of the eclipse. The maximum of the PTV contrast difference of 0.63 occurs at 18:24 UT, which is about 50% higher and occurs 18 min later than in the observations. The shape of the contrast profiles resembles that of a derivative of a Gaussian, switching sign after the culmination of the eclipse. The asymmetries in the lobes and the wings of the contrast profiles are a direct consequence of the eclipse geometry, breaking symmetries related to the CLV and solar differential rotation. In summary, we demonstrated successfully that forward modeling using the Bifrost simulations produces reasonable disk-integrated contrast profiles of the 2017 August 21 eclipse but a more detailed comparison will be carried out in a forthcoming study.

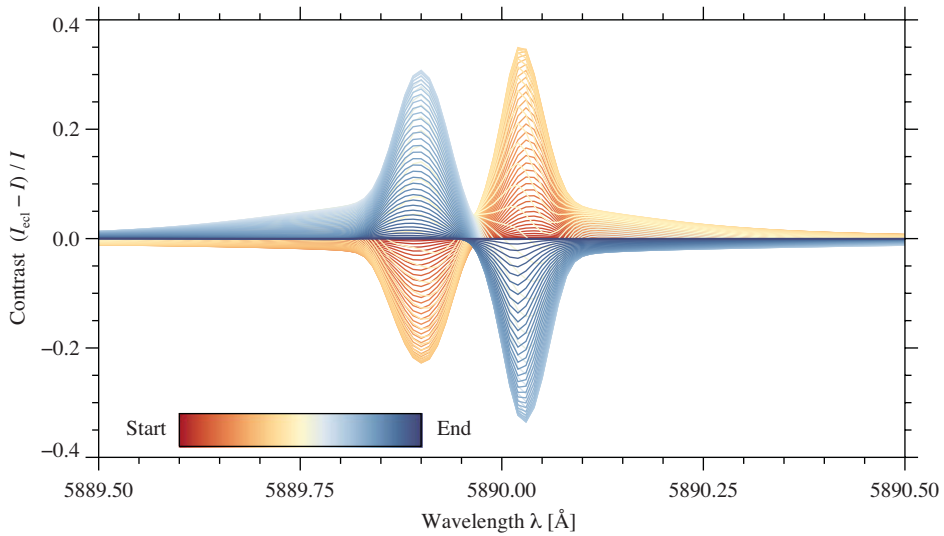


**Figure 5.** Series of contrast profiles covering the 2017 August 21 solar eclipse. The color scale indicate the progress of the partial solar eclipse from start to end as observed at the Mt. Graham Observatory. The contrast profiles were derived from a Bifrost simulation of the CLV of the Na I D<sub>2</sub> intensity profile.

#### 4. Conclusion

The Sun is the only star, where we can obtain high-resolution spectra and spatially resolved images. This allows us to study closely and to quantify with formidable precision phenomena such as convection, magnetic fields, solar activity, and differential rotation. Their detailed examination provides a validation environment connecting solar and stellar physics. Recent advances were made possible by state-of-the-art instruments, facilities, and experiments such as the Synoptic Optical Long-term Investigations of the Sun (SOLIS, Keller *et al.* 2003) program, High Accuracy Radial velocity Planet Searcher (HARPS, Pepe *et al.* 2002), the Calar Alto high-Resolution search for M-dwarfs with Exoearths with Near-infrared and optical Echelle Spectrographs (CARMENES, Quirrenbach *et al.* 2018), and last but not least PEPSI (Strassmeier *et al.* 2015). The last three instruments exploit during nighttime a spectral resolution that rivals high-resolution solar spectroscopy, thus, facilitating close spectral comparisons between the Sun and the stars. Synoptic full-disk data from space missions such as the Solar Dynamic Observatory (SDO, Pesnell *et al.* 2012) enable us to relate spectral signatures from Sun-as-a-star observations to activity and dynamics on the solar disk (e.g., Denker & Verma 2019). In this context, the present study of the 2017 August 21 eclipse serves as an example demonstrating the power of high-resolution Sun-as-a-star spectroscopy.

#### Acknowledgments

PEPSI and SDI were made possible by longtime support of the Bundesministerium für Bildung und Forschung (BMBF) for the collaborative research projects 05AL2BA1/3 and 05A08BAC. This study was supported by grant DE 787/5-1 of the Deutsche Forschungsgemeinschaft (DFG). The support by the European Commission's Horizon 2020 Program under grant agreements 824064 (ESCAPE – European Science Cluster of Astronomy & Particle physics ESFRI research infrastructures) and 824135 (SOLARNET – Integrating High Resolution Solar Physics) is highly appreciated. ED

is grateful for the financial support from the Deutsche Akademische Austauschdienst (DAAD) in form of a doctoral scholarship. This research made use of NASA's Astrophysics Data System (ADS).

## References

- Aimanova, G. K. & Gulyaev, R. A. 1976, *Soviet Astron.*, 20, 201
- Athay, R. G. 1976, *The Solar Chromosphere and Corona: Quiet Sun*, *Astrophys. Space Sci. Lib.*, 53, D. Reidel Publishing Company, Dordrecht, Holland
- Bartlett, J. L., Frouard, M. R. C., Bell, S., *et al.* 2019, in *Celebrating the 2017 Great American Eclipse: Lessons Learned from the Path of Totality*, S. R. Buxner, L. Shore, & J. B. Jensen (eds.), *ASP-CS*, 516, 251
- Bazin, C. & Koutchmy, S. 2013, *J. Adv. Res.*, 4, 307
- Beeck, B., Collet, R., Steffen, M., *et al.* 2012, *A&A*, 539, A121
- Bruls, J. H. M. J., Rutten, R. J., & Shchukina, N. G. 1992, *A&A*, 265, 237
- Cauley, P. W., Kuckein, C., Redfield, S., *et al.* 2018, *Astron. J.*, 156, 189
- Czesla, S., Klocová, T., Khalafinejad, S., *et al.* 2015, *A&A*, 582, A51
- Davis, S. P., Abrams, M. C., & Brault, J. W. 2001, *Fourier Transform Spectrometry*, Academic Press, San Diego, California
- Denker, C. & Verma, M. 2019, *SoPh*, 294, 71
- Dunn, R. B., Evans, J. W., Jefferies, J. T., *et al.* 1968, *ApJSS*, 15, 275
- Gudiksen, B. V., Carlsson, M., Hansteen, V. H., *et al.* 2011, *A&A*, 531, A154
- Habbal, S. R., Druckmüller, M., Morgan, H., *et al.* 2011, *ApJ*, 734, 120
- Haywood, R. D., Collier Cameron, A., Unruh, Y. C., *et al.* 2016, *MNRAS*, 457, 3637
- Hill, J. M., Green, R. F., & Slagle, J. H. 2006, in *Ground-based and Airborne Telescopes*, L. M. Stepp (ed.), *Proc. SPIE*, 6267, 62670Y
- Izumiura, H. 1999, in *Observational Astrophysics in Asia and its Future*, P. S. Chen (ed.), 4, 77
- Keller, C. U., Harvey, J. W., & Giampapa, M. S. 2003, in *Innovative Telescopes and Instrumentation for Solar Astrophysics*, S. L. Keil & S. V. Avakyan (eds.), *Proc. SPIE*, 4853, 194
- Koutchmy, S., Baudin, F., Abdi, S., *et al.* 2019, *A&A*, in press
- Leenaarts, J., Rutten, R. J., Reardon, K., *et al.* 2010, *ApJ*, 709, 1362
- Lendl, M., Cubillos, P. E., Hagelberg, J., *et al.* 2017, *A&A*, 606, A18
- Nikolov, N., Sing, D. K., Gibson, N. P., *et al.* 2016, *ApJ*, 832, 191
- Pasachoff, J. M. 2009, *Nature*, 459, 789
- Pepe, F., Mayor, M., Rupprecht, G., *et al.* 2002, *Messenger*, 110, 9
- Pesnren, W. D., Thompson, B. J., & Chamberlin, P. C. 2012, *SoPh*, 275, 3
- Quirrenbach, A., Amado, P. J., Ribas, I., *et al.* 2018, in *Ground-based and Airborne Instrumentation for Astronomy VII*, C. J. Evans, L. Simard, & H. Takami (eds.), *Proc. SPIE*, 10702, 107020W
- Reiners, A., Lemke, U., Bauer, F., *et al.* 2016, *A&A*, 595, A26
- Rutten, R. J. 2007, in *The Physics of Chromospheric Plasmas*, P. Heinzel, I. Dorotovič, & R. J. Rutten (eds.), *ASP-CS*, 368, 27
- Saito, K. & Tandberg-Hanssen, E. 1973, *SoPh*, 31, 105
- Schleicher, H., Wiedemann, G., Wöhl, H., *et al.* 2004, *A&A*, 425, 1119
- Strassmeier, K. G., Ilyin, I., Järvinen, A., *et al.* 2015, *AN*, 336, 324
- Strassmeier, K. G., Ilyin, I., & Steffen, M. 2018, *A&A*, 612, A44
- Takeda, Y., Ohshima, O., Kambe, E., *et al.* 2015, *PASJ*, 67, 10
- Verma, M. 2018, *A&A*, 612, A101
- Verma, M., Denker, C., Balthasar, H., *et al.* 2016, *A&A*, 596, A3
- Vernazza, J. E., Avrett, E. H., & Loeser, R. 1981, *ApJSS*, 45, 635
- Yan, F., Fosbury, R. A. E., Petr-Gotzens, M. G., *et al.* 2015, *A&A*, 574, A94